Inorganic Chemistry

pubs.acs.org/IC
Article

Synthesis of Amorphous and Various Phase-Pure Nanoparticles of Nickel Phosphide with Uniform Sizes via a Trioctylphosphine-Mediated Pathway

David Thompson, Adam S. Hoffman, Zachary R. Mansley, Sarah York, Feng Wang, Yimei Zhu, Simon R. Bare, and Jingyi Chen*

Cite This: *Inorg. Chem.* 2024, 63, 18981−18991

ABSTRACT: Nickel phosphides are of particular interest because they are highly active and stable catalysts for petroleum/biorefinery and hydrogen production. Despite their significant catalytic potential, synthesizing various phase-pure nickel phosphide nanoparticles of uniform size remains a challenge. In this work, we develop a robust trioctylphosphine (TOP)-mediated route to make highly uniform phase-pure $Ni_{12}P_5$, Ni_2P, and Ni_5P_4 nanoparticles. The synthetic route forms amorphous $Ni_{70}P_{30}$ nanoparticle intermediates. The reactions can be stopped at the amorphous stage when amorphous particles are desired. The amount of P incorporation can be controlled by varying the ratio of TOP to Ni(II). The mechanism for composition control involves the competition of the kinetics of two processes: the addition of the reduced Ni and the incorporation of P into Ni. Uniform $Ni_{70}P_{30}$ amorphous nanoparticles can be generated at a high TOP-to-Ni(II) ratio, where the P incorporation kinetics is made to dominate. $Ni_{70}P_{30}$ can later be transformed into phase-pure $Ni_{12}P_5$, Ni_2P, and Ni_5P_4 nanocrystals of uniform size. The transformation can be controlled precisely by modulating the temperature. A UV−vis study coupled with theoretical modeling reveals Ni(0)-TOP_x complexes along the synthetic path. This approach may be expanded to create other metal compounds, potentially enabling the synthesis of uniform nanoparticles of a greater variety.

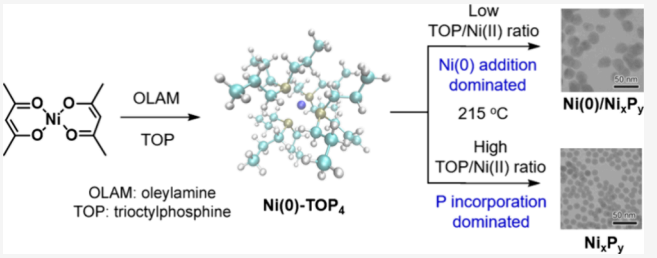

INTRODUCTION

Nickel phosphides are nonprecious metal compounds that are becoming a promising group of highly active and stable catalysts in the petroleum refining industry for hydrodesulfurization (HDS) and hydrodenitrogenation (HDN),[1,2] in biorefinery for hydrodeoxygenation (HDO),[3] and in energy conversion and storage.[4] Their catalytic activity is strongly affected by the phase, size, and morphology of nickel phosphides in these applications such as HDS[5,6] and overall water-splitting reactions.[7−9] A number of methods have been developed for the synthesis of nickel phosphides involving the reactions between nickel salts and different phosphorus sources, including phosphates, hypophosphite, element phosphorus, and phosphines.[8] Among these methods, the wet chemical approach using trioctylphosphine (TOP) as the phosphorus source is an effective means of synthesizing nickel phosphide nanoparticles. The general strategies often involve the thermal decomposition of metal−phosphine intermediates,[10] thermal conversion of metals to phosphides,[11,12] or a one-pot synthesis, combing the metal reduction and phosphorus incorporation.[13−18] For example, Hyeon and coworkers reported that a series of metal−TOP intermediates could be thermally decomposed, leading to the formation of metal phosphide nanoparticles, including solid Ni_2P particles.[10] Schaak and Chiang demonstrated that the thermal conversion of metallic Ni to hollow Ni_2P particles was due to the unequal diffusion rates of Ni and P, known as the Kirkendall effect.[11,12] In the one-pot synthesis, the combination of the reduction of metal precursor and the P incorporation requires the presence of a reducing agent, where oleylamine (OLAM) is often used.

The control of the phase, size, and morphology (hollow versus solid) could be achieved in a one-pot synthesis by varying the reaction parameters, such as the P/Ni precursor ratio, temperature, time, and the amount of OLAM used. For example, Tracy and co-workers showed that at 240 °C, a 1:1 P/Ni ratio formed Ni particles, while a >9:1 P/Ni ratio yielded amorphous Ni_xP_y particles.[14] Further annealing of the Ni and the amorphous Ni_xP_y particles individually generated a crystalline mixture of Ni_2P and $Ni_{12}P_5$, but with different morphologies of hollow versus solid, respectively. Later, Brock

Received: August 5, 2024
Revised: September 14, 2024
Accepted: September 19, 2024
Published: September 27, 2024

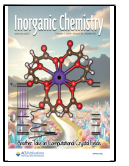

https://doi.org/10.1021/acs.inorgchem.4c03334
Inorg. Chem. 2024, 63, 18981−18991

and co-workers reported that phase-pure $Ni_{12}P_5$ and Ni_2P could be modulated by the TOP quantity, reaction temperature, and heating time.[18] In their study, the void size of the hollow particles could be tuned by the P/Ni precursor ratio and the amount of OLAM used in the synthesis. When phosphidation was performed in the reaction with a large excess of TOP and high temperatures, the products were P-rich phases of Ni_5P_4 and NiP_2.[19] However, the size of the resulting particles was large, typically in the range of 100−500 nm, which appeared to be aggregates consisting of 20−30 nm crystalline nanoparticles. Using a similar TOP-mediated synthesis, monodispersed particles of $Ni_{12}P_5$ (∼20 nm, hollow), Ni_2P (∼10 nm, a mixture of hollow and solid), and Ni_5P_4 (∼600 nm, particle assemblies) were obtained by Liu and co-workers.[20] A theoretical study showed that a clean Ni surface could initiate the P−C bond cleavage of TOP, facilitating the insertion of P to Ni to form nickel phosphides.[21] The energy barriers of the entire process were relatively low, in agreement with the experimental findings, where the birth of nickel phosphides was at a relatively low temperature of 150 °C.[22] Despite these advances of TOP-mediated synthesis, challenges still remain to have complete control over the size, shape, and phase of the nickel phosphide nanoparticles. Further decoupling of the reaction parameters is necessary to understand the reaction mechanism and thus achieve simultaneous control of the morphology and phase for the formation of nickel phosphide nanoparticles.

In this work, we decouple the reaction parameters of the TOP-mediated synthesis, propose a new reaction mechanism, and demonstrate a precise modulation strategy for the formation of phase-pure crystalline $Ni_{12}P_5$, Ni_2P, and Ni_5P_4 nanoparticles with a uniform size. The investigation systematically increases the amount of TOP used in the synthesis of metallic Ni, which was formed by the thermal reduction of nickel(II) acetylacetonate ($Ni(acac)_2$) by using OLAM, to study the TOP effects on the formation of Ni_xP_y. At a relatively low temperature, the P incorporation to the in situ formed metallic Ni results in amorphous phases. The amount of P incorporation mainly depends on the amount of TOP added to the reaction with little influence by the reaction time. Our study shows that the highest P incorporation is approximately 30% at the low reaction temperature, forming uniform $Ni_{70}P_{30}$ amorphous nanoparticles on the order of 10 nm with a standard deviation of less than 2.0 nm. These $Ni_{70}P_{30}$ amorphous nanoparticles can serve as reaction intermediates to the phase-pure crystalline $Ni_{12}P_5$, Ni_2P, and Ni_5P_4 solid nanoparticles with little change in particle size. The key to success is through a two-step heating process, during which the uniform amorphous nanoparticles are formed at the intermediate temperature to facilitate the size and phase purity control of the final products. The as-synthesized nanoparticles can be immobilized to SiO_2 support[6] or metal foil[23] and annealed at elevated temperatures before their use in catalysis. They can also be chemically treated through ligand exchange[24] or covalent surface functionalization[25] before deposition onto carbon support for electrocatalysis. We further employ X-ray absorption spectroscopy (XAS), including both X-ray absorption near-edge spectroscopy (XANES) and extended X-ray absorption fine structure analysis (EXAFS), to analyze the amorphous nanoparticle intermediates from the synthesis. The results, combined with transmission electron microscopy (TEM), X-ray diffraction (XRD), UV−vis spectroscopy, and density functional theory (DFT) calculations, allow us to reveal the Ni(0)-TOP_x involving the reaction mechanism and deepen the understanding of the TOP-mediated nickel phosphides at the nanoscale.

EXPERIMENTAL METHODS

Chemicals and Materials. Nickel(II) 2,4-pentadionate ($Ni(acac)_2$, 95%), tri-n-octylphosphine (TOP, 90%,), chloroform ($CHCl_3$, 99.8%+), toluene, and nitric acid (65−70%, ≥99.999% (metals basis)) were purchased from Alfa Aesar. OLAM (70%), 1-octadecene (ODE, 90%), and acetone were obtained from Sigma-Aldrich. Ethanol (200 proof) was obtained from Koptic. All chemicals were used as received. Ultrapure water was used unless specified.

Synthesis of Crystalline Ni. Crystalline Ni nanoparticles were synthesized by thermal decomposition of the nickel precursor under a reductive environment. In a typical synthesis, $Ni(acac)_2$ (52.4 mg, 0.2 mmol) was added to 5 mL of OLAM in a three-neck round-bottom flask equipped with a Schlenk line under an argon flow. The mixture was then degassed for 10 min under argon. Next, the reaction mixture was heated to 215 °C and held at 215 °C for 15 min. After 15 min, the reaction was quenched by removing the reaction flask from the heating mantle. Once the solution mixture was cooled to 100 °C, the solution was transferred to a 50 mL centrifuge tube, mixed with 3 mL of toluene and 30 mL of ethanol, and centrifuged at 8000 rpm for 5 min. After centrifugation, the supernatant was decanted, and the pellet was purified twice using a 1:10 mixture of toluene and ethanol. The product was dispersed in 3 mL of toluene for future use.

Synthesis of Amorphous Ni_xP_y Nanoparticles. To synthesize the amorphous Ni_xP_y nanoparticles, TOP was added to the synthesis of Ni nanoparticles as a source of phosphorus. Briefly, different amounts of TOP (0.05, 0.2, 0.5, or 1 mL) were added to a three-neck round-bottom flask containing $Ni(acac)_2$ (52.4 mg, 0.2 mmol), 1 mL of OLAM, and 4 mL of ODE. The reaction was heated to 215 °C and held at 215 °C for various periods of time (10, 30, 60, and 120 min). After the specific time for the reaction to proceed, the reaction was quenched, and the resulting nanoparticles were purified using the same procedure as that for the synthesis of crystalline Ni nanoparticles. The product was further purified by acetone and then dispersed in 3 mL of toluene for future use.

Synthesis of Crystalline Ni_2P Nanoparticles. Crystalline Ni_2P nanoparticles were synthesized by using the same procedure as that for the amorphous Ni_xP_y except that an additional heating step at 315 °C was applied to the synthesis. Briefly, $Ni(acac)_2$ (52.4 mg, 0.2 mmol), 1 mL of OLAM, and 4 mL of ODE were added to a three-neck round-bottom flask equipped with a Schlenk line under an argon gas flow. After the mixture was degassed for 10 min under argon, 1 mL of TOP was added to the flask. The reaction mixture was then heated to 215 °C and held at 215 °C for 1 h. After 1 h, the reaction was heated to 315 °C and held at 315 °C for 1 h before the reaction was quenched by removing the reaction flask from the heating mantle. The product collection and purification procedures are the same as those for the amorphous Ni_xP_y nanoparticles.

Synthesis of Crystalline $Ni_{12}P_5$ Nanoparticles. Crystalline $Ni_{12}P_5$ nanoparticles were synthesized by using the same procedure as that for crystalline Ni_2P nanoparticles, except an additional heating step with the temperature held at 280 °C.

Synthesis of Crystalline Ni_5P_4 Nanoparticles. The same procedure as that for the synthesis of crystalline Ni_2P nanoparticles was applied for the synthesis of crystalline Ni_5P_4 nanoparticles, except that the amounts of TOP (1 mL), OLAM (5 mL), and no ODE were used, and the additional heating step was raised to 350 °C and held at 350 °C for 1 h.

Transmission Electron Microscopy Characterization. For TEM sample preparation, each nanoparticle suspension was drop-cast onto a TEM grid and air-dried. Low-magnification TEM images were captured using a JEOL JEM-1011 microscope with an accelerating voltage of 100 kV. High-resolution TEM and high-angle annular dark-field (HAADF)-scanning transmission electron microscopy (STEM) images were acquired using a JEOL ARM200F microscope operated at an accelerating voltage of 200 kV and

https://doi.org/10.1021/acs.inorgchem.4c03334
Inorg. Chem. 2024, 63, 18981−18991

equipped with a cold-field emission gun and CEOS GmbH double C_s aberration correctors. The inner and outer collection angles for the HAADF images used were 68 and 280 mrad, respectively. The two-dimensional electron energy loss spectroscopy (EELS) mapping of the P L-edge was carried out using a Gatan GIF Continuum K3-IS System with the dual-EELS mode used for zero-loss energy-loss calibration. A power-law background subtraction was applied, and the data were processed using principal component analysis to reduce noise.

X-ray Diffraction Characterization. To prepare the samples for XRD, each nanoparticle sample was precipitated by centrifugation, and the solid was dried under a nitrogen flow. The solid sample was placed on an XRD polymer loop that was mounted on a holder. XRD was performed using an X-ray diffractometer (Rigaku XtalLab Synergy) operated at 50 kV and 1 mA with Cu Kα radiation as the source.

Inductively Coupled Plasma Mass Spectrometry Characterization. For inductively coupled plasma mass spectrometry (ICP-MS) sample preparation, 143 μL of concentrated HNO_3 was added to each dry sample in a 2dr vial to digest the sample. The solution containing the digested sample was then diluted to 5 mL by using H_2O to yield the final matrix concentration of 2% HNO_3. The concentrations of Ni and P in each sample were obtained from ICP-MS (Thermo Fisher iCAP TQ). The linear ranges used for the calibration curve for Ni and P are 1−1000 and 50−1000 ppb, respectively.

UV−Vis Spectroscopy Study. The reaction was carried out at the same conditions as the synthesis of amorphous Ni_xP_y nanoparticles, with 1 mL of TOP used. During the course of the reaction, a 10 μL aliquot was sampled from the reaction and diluted in 2 mL of ODE in a quartz cuvette with a sealed cap for UV−vis measurements at different time points. The UV−vis spectra were recorded using a UV−vis spectrophotometer (Agilent Cary 50, Santa Clara, CA, USA), scanned from 200 to 800 nm at a scan rate of 10 nm per second.

The molecular structures were built using the GaussView graphical interface and optimized using ORCA,[26] with density fitting DFT using Becke's 3-parameter Lee−Yang−Parr (B3LYP) exchange−correlation functional.[27] The Coulombic and exchange integrals were approximated with the RIJCOSX algorithm.[28] Geometry optimization was performed with the def2-SVP[29] basis set. However, a larger def2-TZVP basis set was used to compute the UV spectra with time-dependent DFT. The geometry optimization was performed in vacuum, assuming both singlet and triplet ground states. The singlet configuration was found to be more stable for all of the compounds reported. The UV spectra were computed with the singlet ground state in an implicit solvent of toluene approximated with the conductor-like polarizable continuum model.[29] A total of 15 states were considered for computing the UV spectra.

X-ray Absorption Spectroscopy Characterization. Each sample (~60 μg/cm^2, 0.5 cm diameter circle) was sandwiched between two pieces of Kapton tape. Ni K-edge XAS data were collected at beamline 4-1 of the Stanford Synchrotron Radiation Lightsource (SSRL) at SLAC National Accelerator Laboratory. These samples were placed in the beam path perpendicular to the incident X-ray beam. The transmission signal was collected for the Ni K-edge (8333.0 eV). Energy calibration was achieved by simultaneously scanning a Ni foil with each sample. Data calibration and analysis were carried out using the Demeter software package.[30] The absorption edge energy for the Ni K-edge was calibrated to 8333.0 eV, and the EXAFS models were optimized in R-space using k^1, k^2, and k^3 weightings, obeying the Nyquist criterion. The amplitude reduction factor (S_0^2) was determined by modeling the EXAFS spectra of the pure metallic Ni to be 0.75. The following Fourier transform (FT) parameters were chosen: k_{min} = 2.5 Å^{-1}, k_{max} = 14 Å^{-1} for $Ni_{98}P_2$ and $Ni_{95}P_5$; k_{min} = 2.5 Å^{-1}, k_{max} = 13 Å^{-1} for $Ni_{90}P_{10}$, $Ni_{85}P_{15}$, and $Ni_{80}P_{20}$; k_{min} = 2.5 Å^{-1}, k_{max} = 10 Å^{-1} for $Ni_{75}P_{25}$ and $Ni_{70}P_{30}$; dk = 1, r_{min} = 1 Å, r_{max} = 3.0 Å, and dr = 0 with k-spline at 15 Å^{-1} were used for all of the samples. A simultaneous fitting approach using scattering paths chosen from metallic Ni[31] (Ni−Ni) and Ni_2P[32] (Ni−Ni and Ni−P) was used to model Ni EXAFS spectra for all of the samples, where $Ni_{98}P_2$ and $Ni_{95}P_5$ were only fitted with metallic Ni−Ni, while others were fitted with all three paths. In this approach, for the Ni−Ni path of metallic Ni, the samples shared the same ΔE, σ^2, and R. The CN was fitted individually. Similarly, this setting was also applied for the Ni−Ni and Ni−P paths from Ni_2P with the exception of ΔE, which was shared for both paths. A total of 25 parameters (2 ΔE, 3 σ^2, 3 R, and 17 CN) were fitted in the EXAFS modeling.

RESULTS AND DISCUSSION

Nickel phosphides were synthesized through the incorporation of P obtained from TOP to the Ni generated in situ from the thermal reduction of $Ni(acac)_2$ by OLAM. The reaction scheme is illustrated in Figure 1A. In the absence of TOP,

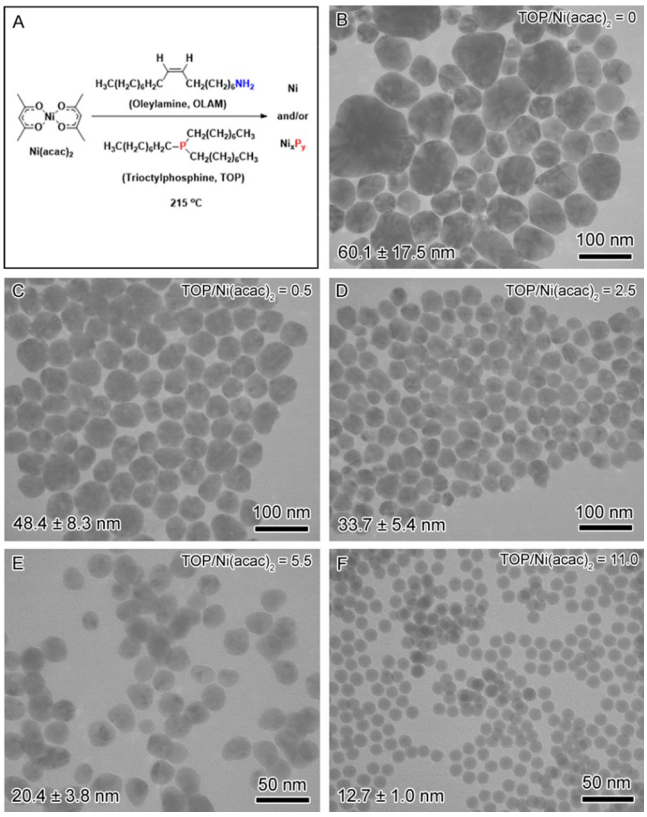

Figure 1. (A) Reaction scheme of the chemical approach to amorphous Ni_xP_y via phosphorus insertion. (B) TEM image of Ni nanoparticles synthesized at 215 °C for 60 min via reduction of $Ni(acac)_2$ in OLAM without the presence of TOP. (C−F) TEM images of the products from the reactions under the same conditions at 215 °C for 60 min but varying the molar ratio of TOP/$Ni(acac)_2$: (C) 0.5; (D) 2.5; (E) 5.5; and (F) 11.0.

$Ni(acac)_2$ could be reduced by OLAM to Ni at 215 °C. The reaction mixture started as an opaque light blue color due to insoluble $Ni(acac)_2$ suspended in OLAM at room temperature. Upon heating to 40 °C, $Ni(acac)_2$ is fully dissolved under magnetic stirring, and the mixture turns translucent light green. By heating continuously to 215 °C, the reaction mixture gradually becomes translucent dark green and remains dark green until 15 min at 215 °C, at which point the mixture turns to opaque dark black, indicating the formation of Ni nanoparticles. The observation matches with the previous study of the reduction of $Ni(acac)_2$ by OLAM.[33] The mechanism for the reaction was proposed to undergo a two-

https://doi.org/10.1021/acs.inorgchem.4c03334
Inorg. Chem. 2024, 63, 18981−18991

electron chemical reduction route,[33] as opposed to a thermolysis[34] or a radical reaction.[35]

In the presence of TOP, Ni_xP_y is formed by replacing Ni on the Ni surface.[22] At a TOP/$Ni(acac)_2$ ratio of 0.5, the reaction mixture turns opaque dark black at the time similar to that of the Ni synthesis—15 min after the reaction mixture is heated to 215 °C. As the TOP/$Ni(acac)_2$ ratio increases, the temperature at which the reaction mixture turns opaque dark black decreases, occurring at 215, 205, and 185 °C, for ratios of 2.5, 5.5, and 11.0, respectively. This suggests that the increased amount of TOP in the reaction lowers the energy barrier for the nanoparticles to form. After the reaction temperature was ramped to 215 °C, all of the reactions proceeded at 215 °C for 60 min. Figure 1B–F displays the TEM characterization of the products from the thermal reduction of Ni in the absence and in the presence of TOP indicated by the TOP/$Ni(acac)_2$ ratio of 0, 0.5, 2.5, 5.5, and 11.0. The corresponding atomic compositions of the products were measured by ICP-MS to be pure Ni, $Ni_{99}P_1$, $Ni_{95}P_5$, $Ni_{86}P_{14}$, and $Ni_{72}P_{28}$, respectively. As shown in the TEM images, the size of the particles decreases from 60.1 ± 17.5 nm (pure Ni) to 48.4 ± 8.3 nm ($Ni_{99}P_1$), 33.7 ± 5.4 nm ($Ni_{95}P_5$), 20.4 ± 3.8 nm ($Ni_{86}P_{14}$), and 12.7 ± 1.0 nm ($Ni_{72}P_{28}$). The size distribution becomes narrower, and the morphology changes from an irregular to a spherical shape as the P content increases in these samples. In other words, an increase of the TOP/$Ni(acac)_2$ ratio in the synthesis facilitates the formation of uniform small solid nanoparticles with a higher P content.

To determine the corresponding crystalline phases, the XRD patterns of these samples were obtained, as shown in Figure 2.

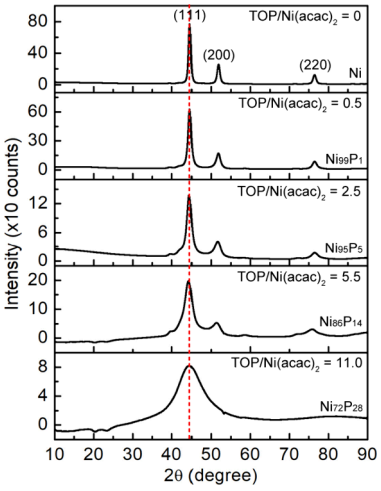

Figure 2. XRD of the samples that are depicted in Figure 1. The degree of crystallinity decreases with an increased ratio of TOP/$Ni(acac)_2$ in the synthesis from the top to the bottom corresponding to the samples (Figure 1B–F). The pure Ni is indexed to an *fcc* crystal structure of Ni (ICDD-JCPDS card no. 04-0850). The compositions are the results obtained from ICP-MS.

The XRD pattern of the pure Ni sample exhibits peaks at 44.5°, 51.9°, and 76.5° that can be indexed to the (111), (200), and (220) crystallographic planes of a face-centered cubic (*fcc*) structure of metallic Ni. The XRD patterns of these samples for $Ni_{99}P_1$, $Ni_{95}P_5$, and $Ni_{86}P_{14}$ are similar to those of the metallic Ni, as indicated by the presence of three major peaks at 44.5°, 51.9°, and 76.5°, but the peaks become broader as the P content increases. For $Ni_{72}P_{28}$, the broadening causes the convolution of the first two peaks of 44.5° and 51.9° and the disappearance of the weak peak of 76.5°, leaving only the peak at 44.5° in its XRD pattern. The peak broadening could be attributed to the reduced size and the reduced crystallinity of the particles due to the presence of P.

We employed high-resolution TEM (HRTEM) and EELS mapping to analyze the phases at the single particle level. The TEM image in Figure 3A displays two particles in the $Ni_{85}P_{15}$ sample: one that is made up of an amorphous domain and a crystalline *fcc* Ni domain, while the other consists of crystalline *fcc* Ni. The EELS mapping in Figure 3B indicates that P is present only in the amorphous domain of the particles. The coexistence of crystalline Ni and amorphous Ni_xP_y in a sample suggests that the addition of the reduced Ni and the incorporation of P to Ni simultaneously occur during the reaction. However, the rate of each process depends on the ratio of TOP/$Ni(acac)_2$. When the ratio of TOP/$Ni(acac)_2$ is small (e.g., ≤2.5), the addition of the reduced Ni dominates. At a ratio of TOP/$Ni(acac)_2$ = 5.5, the rates of the reduced Ni addition and the P incorporation are equal, resulting in a heterogeneous mixture of pure Ni and Ni/Ni_xP_y phase-segregated nanoparticles. When the ratio of TOP/$Ni(acac)_2$ is large (e.g., = 11), the P incorporation outcompetes the addition of reduced Ni, resulting in amorphous Ni_xP_y nanoparticles that lack long-range order. However, this cannot rule out the presence of very tiny crystallite Ni in the amorphous Ni_xP_y nanoparticles.

It appears that the competing pair of reactions, the addition of reduced Ni and the replacement of Ni by P, affects the synthesis product. We further investigated the effects of reaction time and the ratio of TOP/$Ni(acac)_2$ on the morphology and composition of the products. The results of TEM and XRD are shown in Figures 4 and 5, respectively. The ratios of Ni to P for the samples obtained from ICP-MS analysis are listed in Table S1. The particles with an average size of >20 nm have a set of peaks in their XRD patterns that can be indexed to metallic Ni. In contrast, the particles close to 10 nm are amorphous in nature with only one peak at 44.5° and their composition is very near $Ni_{70}P_{30}$. For comparison, we included the particle size measured from TEM and the Ni/P atomic ratio derived from ICP-MS results in Table S2.

From these results, we note some general aspects that affect the outcome of the synthesis. At a low TOP/$Ni(acac)_2$ ratio of 2.5, the products are mainly crystalline Ni particles with less than 5% P, whereas at a high TOP/$Ni(acac)_2$ ratio of 11.0, the products are largely amorphous small Ni_xP_y particles with ∼25% P, regardless of the reaction time. At a moderate TOP/$Ni(acac)_2$ ratio of 5.5, the products evolve from large crystalline Ni particles with 6% P content at 10 min to the same-sized crystalline Ni particles containing 13% P content at 30 min and finally small amorphous Ni_xP_y particles with 24% P content at 120 min. However, when TOP/$Ni(acac)_2$ is reduced to 0.5, there is no product that could be isolated for characterization at 10 min, but we were able to obtain small amorphous particles with 28% P at 30 min and large crystalline Ni particles with 2% P at 120 min. These observations suggest that the presence of Ni atoms facilitates the cleavage of P from TOP to form Ni–P at the initial stage of the synthesis. The formation of Ni_xP_y, in turn, promotes the reduction of Ni(II) to Ni. As the synthesis proceeds, if there is insufficient TOP in the reaction, the addition of reduced Ni will dominate the replacement of Ni by P, resulting in the crystalline Ni particles with only a small amount of P incorporation. However, if

https://doi.org/10.1021/acs.inorgchem.4c03334
Inorg. Chem. 2024, 63, 18981–18991

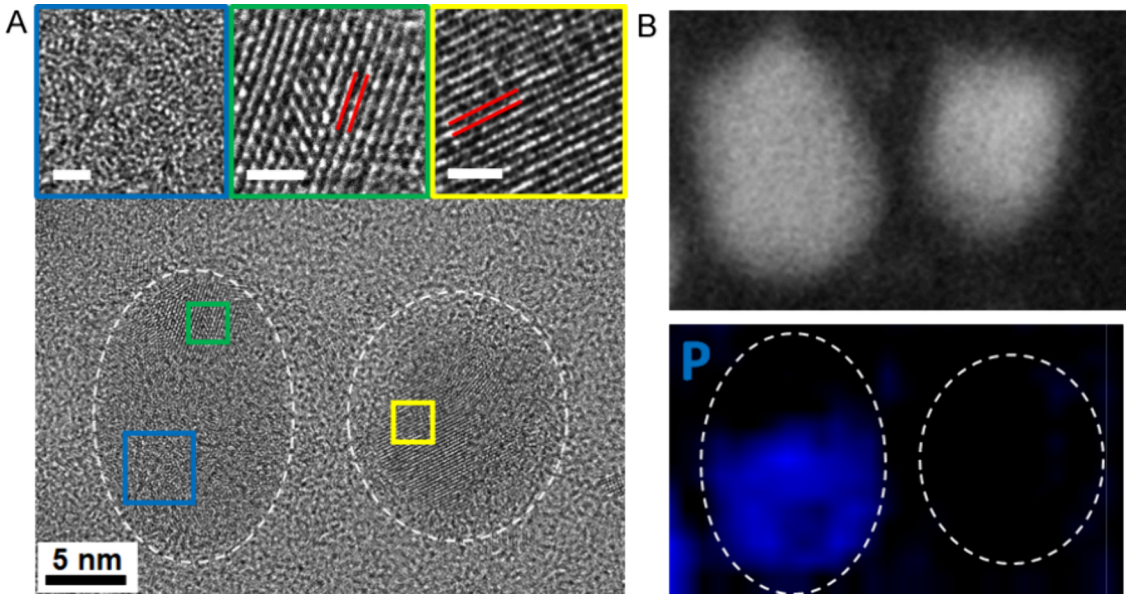

Figure 3. (A) HRTEM image of two nanoparticles from the $Ni_{85}P_{15}$ sample, which are circled in white, indicating a mixture of crystalline and amorphous domains. Magnified colored insets corresponding to the colored boxes on the image reveal an amorphous structure in the bottom half of the left-hand particle and crystalline domains in the top of the left-hand particle and in the right-hand particle (inset scale bars are 1 nm). In both cases, the lattice spacing indicated with red lines corresponds to Ni {111} (0.21 nm). (B) HAADF-STEM image and the EELS map showing phosphorus is mainly located within the amorphous regions of the nanoparticles.

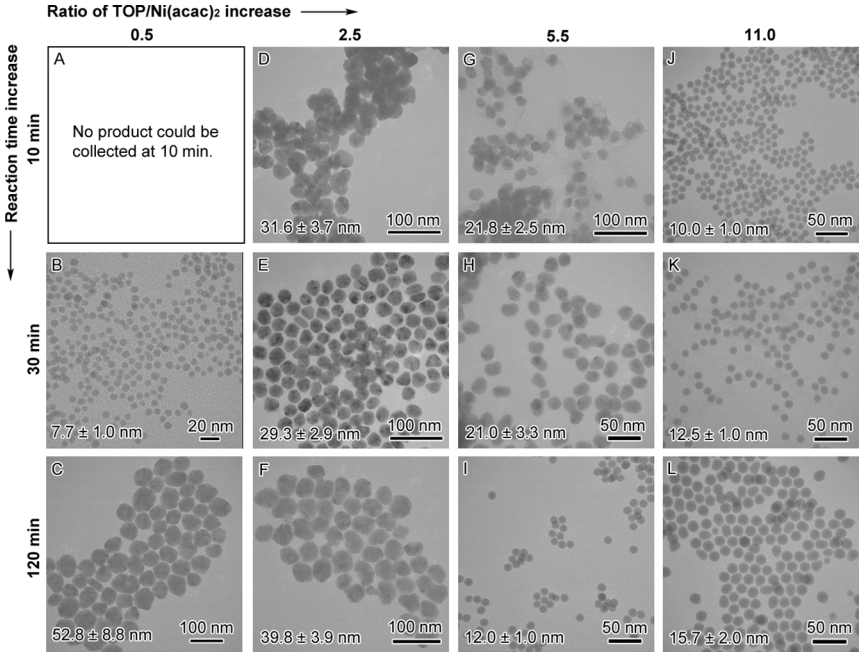

Figure 4. TEM images of the products from the TOP/$Ni(acac)_2$ ratio and reaction time-dependent study under the same conditions at 215 °C: (A) 0.5, 10 min; (B) 0.5, 30 min; (C) 0.5, 120 min; (D) 2.5, 10 min; (E) 2.5, 30 min; (F) 2.5, 120 min; (G) 5.5, 10 min; (H) 5.5, 30 min; (I) 5.5, 120 min; (J) 11.0, 10 min; (K) 11.0, 30 min; and (L) 11.0, 120 min.

sufficient TOP is in the reaction, P will replace Ni to form small amorphous Ni_xP_y nanoparticles with a higher percentage of P content. As the particles become smaller, the peak of the XRD pattern begins to be broad; however, there were no new sets of peaks formed that could be indexed to nickel phosphide crystalline phases. A further increase of the TOP/$Ni(acac)_2$ ratio to 56 and the maximum 66 (used 6 mL of TOP alone) reduced the size of particles to 5.0 ± 1.0 and 3.8 ± 0.6 nm, respectively. Nonetheless, there were little changes to their composition (i.e., 69/31 Ni/P ratio or $Ni_{69}P_{31}$) and XRD patterns (i.e., one broad peak at 44.5°). The results are included in Figure S4. Therefore, we conclude that the nickel phosphides formed under these reaction conditions were amorphous. The results agree with the previously reported literature.[16,18]

In order to gain additional insight into the structure of Ni nanoparticles with P incorporation,[36,37] we employed XAS to obtain local structural information around Ni in these samples. A series of Ni_xP_y samples with the P content increasing from 2 to 30% measured by ICP-MS was chosen for the XAS study.

https://doi.org/10.1021/acs.inorgchem.4c03334
Inorg. Chem. 2024, 63, 18981−18991

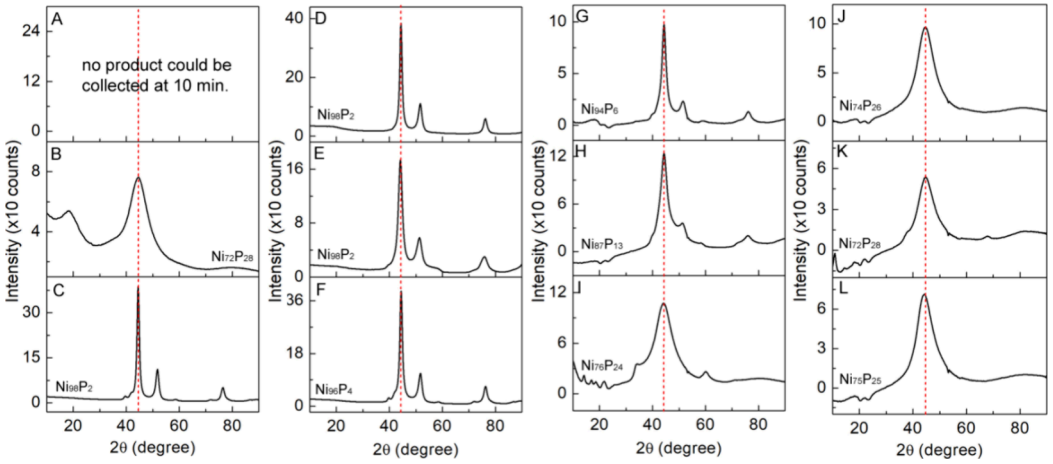

Figure 5. XRD of the corresponding samples that are shown in Figure 4. (A–L) Compositions are the results obtained from ICP-MS. The dashed line in red is the peak position corresponding to the (111) plane of the Ni XRD patterns.

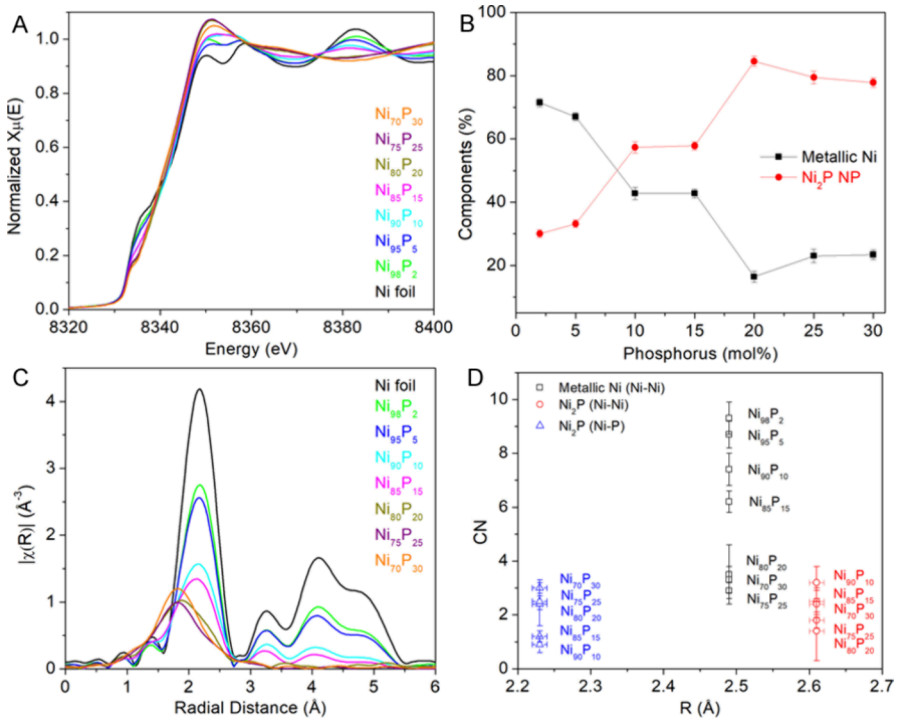

Figure 6. Ni K-edge XAS data of the Ni_xP_y nanoparticles with different compositions: (A) Ni K-edge XANES spectra; (B) plot of percent distribution of metallic Ni and Ni_2P obtained by LCF analysis; (C) Ni K-edge k^2-weighted magnitude of the FT EXAFS spectra; and (D) Ni coordination number (CN) vs bond length (R).

Figure 6A displays a comparison of the Ni K-edge XANES spectra of the samples. The weak pre-edge feature arises from electric quadrupole transition from 1s → 3d of Ni.[38] The intensity of this pre-edge feature at 8335.0 eV decreases with an increased P content from 0 to 15%. The pre-edge intensity can reflect the ratio of unoccupied 3d orbitals.[38,39] The decrease in intensity corresponds to the increase of electron density of Ni due to the electron transfer from P atoms to Ni atoms for P content less than 15%, which agrees with the previous XAS study on the amorphous Ni_xP_y alloys.[39] As the P content increases in the range of 20–30%, the pre-edge peak shifts to 8334.0 eV. The small variation in peak intensity could be attributed to the coordination number and geometry.[38] The XANES of Ni_xP_y ($y \leq 15$) closely resembles that of metallic Ni. As y increases to 20–30%, the shape of the near edge changes from two peaks with a valley to a single peak, which slightly shifts toward higher energy as the P content increases, an indication of electron transfer from Ni to P, resulting in an increase in the oxidation state of Ni. The analysis of HRTEM and EELS mapping allows us to identify that these nanoparticle samples may contain two components—metallic nickel and nickel phosphide. We, therefore, performed linear combination fitting (LCF) on the XANES data of these nanoparticle samples using the XANES data of metallic Ni and bulk crystalline Ni_2P, as shown in Figures 6B and S1. As the amount of P increases, the metallic Ni component decreases; however, the relationship is not linear. The Ni and P percentages for each sample derived from the LCF results are listed in Table S3. Compared to the ICP-MS results, there is about a 5%

https://doi.org/10.1021/acs.inorgchem.4c03334
Inorg. Chem. 2024, 63, 18981–18991

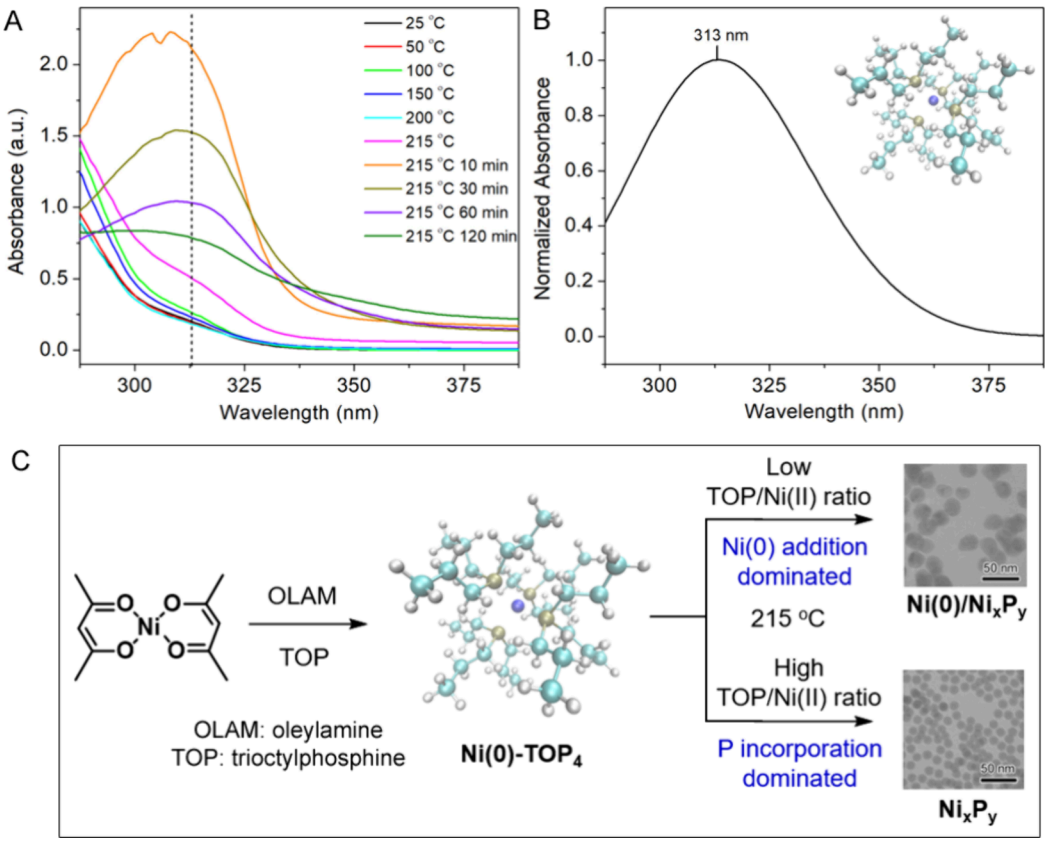

Figure 7. (A) UV−vis spectra of the aliquots taken from the reaction for the synthesis of the amorphous Ni_xP_y with 1 mL of TOP used; (B) calculated UV−vis spectrum (λ_{max} = 313 nm) of a tetrahedral Ni(0)-TOP_4 complex shown in the inset; and (C) schematic illustration of the reaction mechanism for the TOP-mediated synthesis.

discrepancy, which overestimates the P content at low concentrations but underestimates it at high concentrations.

We further performed modeling of the Ni K-edge EXAFS data to understand the coordination environment of Ni, including the bond length (R) and coordination number (CN) in these amorphous samples. Figure 6C displays the Ni K-edge k^2-weighted magnitude of the FT EXAFS spectra. Compared to the Ni foil, changes can be seen for the peak resulting from the first scattering path of these samples. For P < 10%, the position and shape of the peak align with those of the Ni foil, but the intensity decreases by one-third. As the P content increases to 15%, the position of the first peak remains similar, while the intensity further decreases to one-third of the foil and the peak becomes broadened. With an incorporation of P to Ni of 20−30%, the position of the first peak shifts to a shorter distance and the shape of the peak is broader. In order to determine the number of phases present in these samples, we applied the continuous Cauchy wavelet transform (CCWT) tool,[40−43] as shown in Figure S2. The 2 and 5% P-incorporated samples exhibit patterns similar to those of the Ni foil, which contains mainly one component in the first shell. We thus modeled these two samples with only the scattering path (Ni−Ni, R = 2.49 Å, CN = 12) from metallic Ni.[31] At 10% P, an additional component is visible in the CCWT, and the intensity of this component becomes stronger as the percentage of P increases. Based on the HRTEM and EELS mapping results, we attribute this to the presence of amorphous nickel phosphides. Therefore, the EXAFS spectra of the samples with $P \geq 10\%$ were modeled with both a Ni−Ni path from metallic Ni[31] and a Ni−P path (R = 2.21 Å, CN = 2) and a Ni−Ni path (R = 2.61 Å, CN = 4) from Ni_2P.[32]

The modeling results are listed in Table S4 and plotted in Figures 6D and S3. The CNs of metallic Ni are 9.3 ± 0.6 and 8.7 ± 0.5 at 2 and 5% P incorporated into the nanoparticles, respectively. The reduction of the CN from the bulk value (12) is likely due to P incorporation. For comparison, we also fitted these two samples using the paths from both phases. The CNs for Ni−P are 0.4 ± 0.3 and 0.3 ± 0.2 for $Ni_{98}P_2$ and $Ni_{95}P_5$, close to the calculated values of 0.4 and 0.6, assuming a homogeneous mixture and the P substitution of Ni in a *fcc* metallic phase.[44] The result is also similar to the previously reported value for $Ni_{95}P_5$ (i.e., 0.6).[36] When the percentage of P incorporation increases, the CN of metallic Ni continues to decrease to 7.4 ± 0.6, 6.2 ± 0.4, and 3.5 ± 1.1, for 10, 15, and 20% P incorporation, respectively, and then levels off at around 3 for 25 and 30% P incorporation. Meanwhile, the CN for Ni−P increases from 0.9 ± 0.3 to 3.0 ± 0.3 as the amount of P increases in the nanoparticles. Interestingly, the CN for Ni−Ni from Ni_2P first decreases from 3.2 ± 0.6 at 10% P to 1.4 ± 1.1 at 20% P and then increases back up to 2.4 ± 0.5 at 30% P. It is worth noting that the $Ni_{90}P_{10}$, $Ni_{85}P_{15}$, and $Ni_{80}P_{20}$ nanoparticles were synthesized using a TOP/$Ni(acac)_2$ ratio of 5.5, with increased reaction times from 10, 30, and 120 min, while the $Ni_{75}P_{25}$ and $Ni_{70}P_{30}$ nanoparticles were prepared using the TOP/$Ni(acac)_2$ ratio of 11 with 10 and 60 min, respectively. With an increased reaction time, more P was incorporated into the nanoparticles in both cases. The rate of the P incorporation increases with an increased ratio of TOP/$Ni(acac)_2$.

https://doi.org/10.1021/acs.inorgchem.4c03334
Inorg. Chem. 2024, 63, 18981−18991

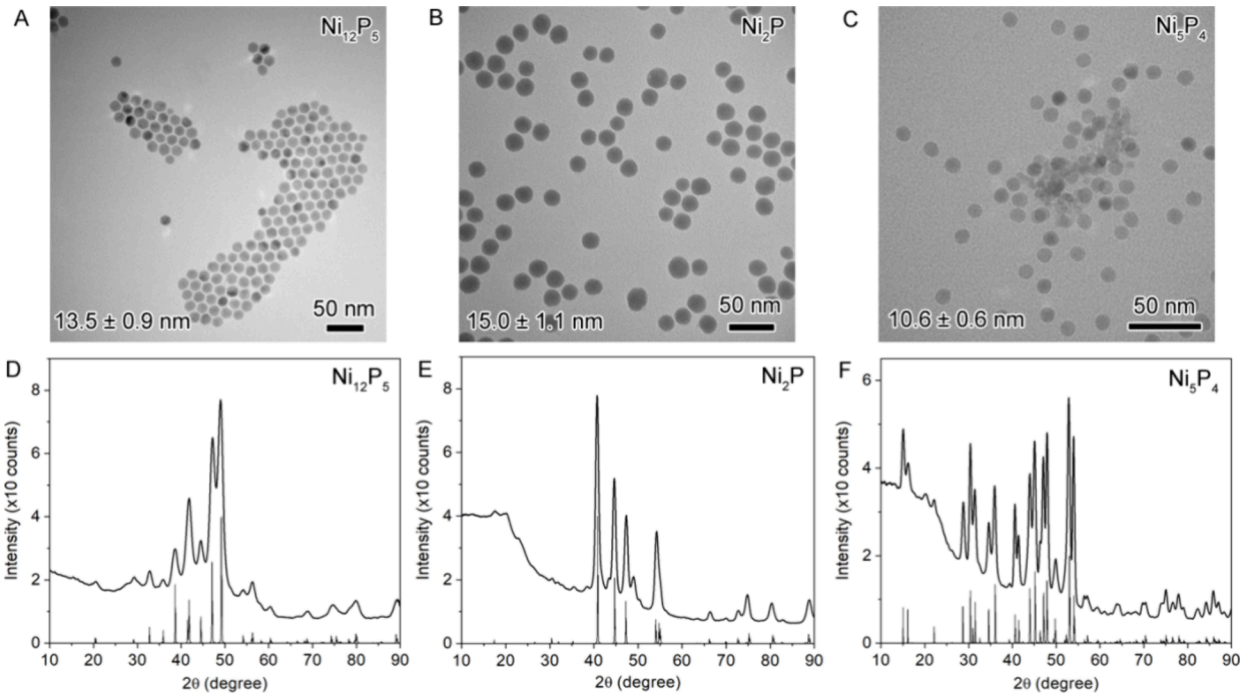

Figure 8. TEM and XRD characterization of phase-pure crystalline nanoparticles of $Ni_{12}P_5$, Ni_2P, and Ni_5P_4: (A–C) TEM images and (D–F) XRD patterns.

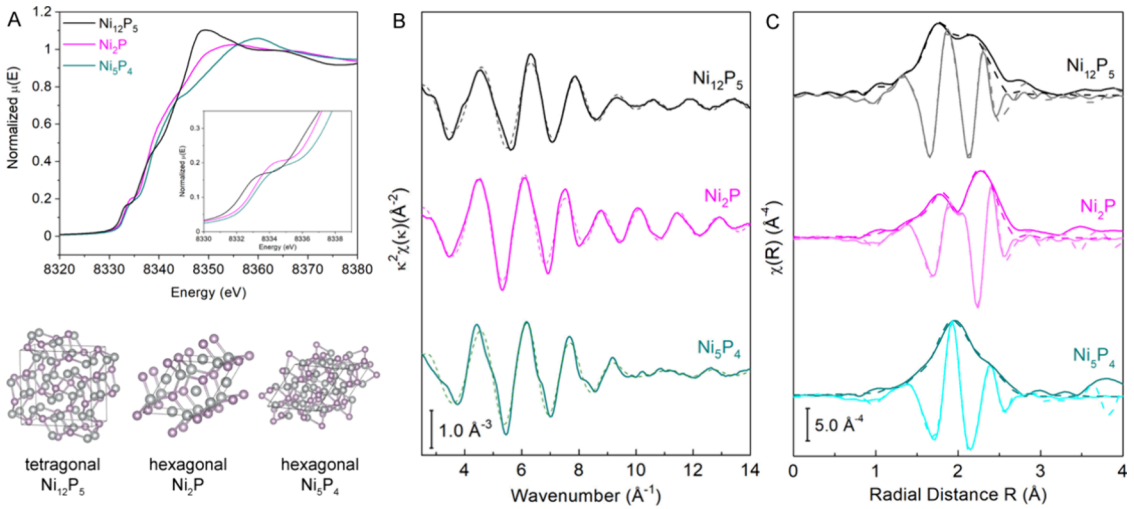

Figure 9. XAS characterization of phase-pure crystalline nanoparticles of $Ni_{12}P_5$, Ni_2P, and Ni_5P_4: (A) Ni K-edge XANES spectra with the corresponding crystal structures; (B) Ni K-edge EXAFS data in K space with their corresponding fits (dashed lines); and (C) Ni K-edge EXAFS data in R space with the real (brightly colored) and imaginary (faded color) components for $Ni_{12}P_5$ (black), Ni_2P (magenta), and Ni_5P_4 (cyan) with their corresponding fits (dashed lines).

To further understand the reaction mechanism, the reaction with a TOP/$Ni(acac)_2$ ratio of 11 was monitored by UV–vis spectroscopy. Small aliquots (10 μL) were taken during the course of the synthesis and diluted in 2 mL of solvent (i.e., ODE) for UV–vis measurements. The spectra are plotted in Figure 7A. A shoulder band started to rise at about 310 nm when the reaction mixture was heated to 100 °C. The band became more pronounced as the reaction temperature was increased to 215 °C and gradually evolved to a broad peak after the reaction had been allowed to proceed at 215 °C for 10 min. From this point, the intensity of the peak decreased with a further increased reaction time at 215 °C until the reaction was stopped at 120 min. We hypothesize that this peak could be associated with the electronic excitation of the Ni-TOP complexes present in the reaction. To verify this hypothesis, we used DFT to simulate the UV–vis spectrum of the complex. Figure 7B displays the TDDFT spectrum of a tetrahedral Ni(0)-TOP_4 complex at the optimized geometry. The calculated spectrum shows a broad band at λ_{max} = 313 nm, which matches the peak position of the experimental spectra. Based on this finding, a reaction mechanism is proposed in Figure 7C, involving the intermediate Ni(0)-TOP_4 complex. The reaction mechanism was further verified by reacting bis(1,5-cyclooctadiene)nickel(0) ($Ni(COD)_2$) with TOP based on the hypothesis that the COD ligand would be replaced by TOP to form Ni(0)-TOP. The equivalent amount

https://doi.org/10.1021/acs.inorgchem.4c03334
Inorg. Chem. 2024, 63, 18981–18991

of $Ni(COD)_2$, as that was used for $Ni(acac)_2$ (0.2 mmol), was dispersed in 6 mL of TOP in a three-neck round-bottom flask under argon. The reaction mixture was heated to 215 °C and monitored by UV−vis spectroscopy. The absorbance peak at ∼313 nm that can be assigned to the Ni(0)-TOP_4 complex appears as soon as $Ni(COD)_2$ is mixed with TOP and becomes more obvious as the temperature increases to 215 °C (Figure S5). The UV−vis spectrum of $Ni(COD)_2$, before TOP was introduced, shows a broad peak at 300 nm different from that of Ni(0)-TOP_4. This experiment provides strong supporting evidence for our interpretation of UV−vis spectra. In addition, we calculated the UV−vis spectrum of Ni(II)-TOP_4, which shows two peaks at 252 and 325 nm. This result also strongly supports that the single peak near 313 nm is characteristic of Ni(0). The composition of the product depends on the TOP/$Ni(acac)_2$ ratio. At low TOP/$Ni(acac)_2$ ratios, the product was dominated by metallic Ni, while uniform amorphous Ni_xP_y nanoparticles were formed at high TOP/$Ni(acac)_2$ ratios.

Since the reaction with the TOP/$Ni(acac)_2$ ratio of 11 yields uniform nanoparticles with a size on the order of 10 nm, we further investigated the effect of the temperature on the reaction. At 215 °C, the reaction yields amorphous Ni_xP_y with an atomic Ni/P ratio of ∼75/25. Extending the reaction to 2 h, the composition slightly changes to $Ni_{70}P_{30}$ and the product remains amorphous. We hypothesize that elevating the temperature can promote the P incorporation and enhance crystallinity to access phase-pure crystalline nanoparticles with a similar size. To test the hypothesis, we carried out the reaction under the same conditions, except that after being kept at 215 °C for 1 h, the reaction was heated to a series of higher temperatures and annealed at that temperature for another hour. Through annealing at 280 °C, the reaction resulted in $Ni_{12}P_5$ nanoparticles, while at 315 and 350 °C, the reaction yielded Ni_2P and Ni_5P_4 nanoparticles, respectively. As seen in the TEM images (Figure 8A−C), these crystalline nanoparticles have a similar size in the range of 10−15 nm. The XRD patterns in Figure 8D−F indicate that the samples are phase-pure, corresponding to $Ni_{12}P_5$,[45] Ni_2P,[32] and Ni_5P_4.[46]

We further characterized these phase-pure nanoparticles with a similar size by XAS. Figure 9A displays the Ni K-edge XANES comparison along with the crystal structures of the three phases—$Ni_{12}P_5$,[45] Ni_2P,[32] and Ni_5P_4.[46] $Ni_{12}P_5$ belongs to the tetragonal crystal system with two inequivalent $Ni^{1.25+}$ ions, while Ni_2P and Ni_5P_4 are associated with the hexagonal crystal system and contain a mixture of Ni^+, Ni^{2+}, and Ni^{3+}. As XANES is sensitive to the oxidation state and coordination environment (e.g., geometry), the XANES region of these three phases is quite different from each other but are similar to those reported in the literature for the corresponding nanoscale $Ni_{12}P_5$,[47] Ni_2P,[48−52] and Ni_5P_4.[50,53] The pre-edge feature of $Ni_{12}P_5$ at 8333.0 eV slightly shifts down 1 eV from those of Ni_2P and Ni_5P_4 at 8334.0 eV, probably due to a NiP_4 tetrahedral geometry dominated in the $Ni_{12}P_5$ phase versus a NiP_5 trigonal bipyramid dominated in Ni_2P and Ni_5P_4 crystal structures. The EXAFS regions of these three nanoparticle samples were modeled using Ni−P and Ni−Ni scattering paths from their corresponding crystal structures $Ni_{12}P_5$,[45] Ni_2P,[32] and Ni_5P_4.[46] The fitting results are plotted in Figure 9B,C and are listed in Table S5. The Ni−P bond distances of all three nanoparticle samples (i.e., 2.21 ± 0.03, 2.24 ± 0.02, and 2.29 ± 0.01 Å for $Ni_{12}P_5$, Ni_2P, and Ni_5P_4, respectively) are similar to those of their bulk structures (i.e., 2.22, 2.21, and 2.30 Å for $Ni_{12}P_5$, Ni_2P, and Ni_5P_4, respectively). For the Ni−Ni bond length, the Ni_2P nanoparticle sample has an average of 2.60 ± 0.01 Å similar to that of the bulk (2.61 Å), while $Ni_{12}P_5$ and Ni_5P_4 nanoparticle samples show 1.5 and 2.6% contractions compared to those of the bulk structures (2.50 ± 0.02 vs 2.54 Å for $Ni_{12}P_5$ and 2.58 ± 0.01 vs 2.65 Å for Ni_5P_4). The contraction is likely associated with the average size difference, as the size of the crystalline nanoparticles decreases in the order of Ni_2P (15.0 ± 1.1 nm), $Ni_{12}P_5$ (13.5 ± 0.9 nm), and Ni_5P_4 (10.6 ± 0.6 nm).

CONCLUSIONS

We have systematically studied the TOP-mediated synthesis of nickel phosphide nanoparticles, proposed a new reaction mechanism, and demonstrated a simple temperature-modulation means to synthesize phase-pure crystalline nanoparticles with a narrow size distribution. At a reaction temperature of 215 °C, the P incorporation into metallic Ni nanoparticles resulted in the formation of amorphous nickel phosphides. The reaction involved two competing processes: the addition of Ni(0) forming metallic Ni and the incorporation of P to the metallic Ni, yielding disordered nickel phosphides. The kinetics of these two processes depended on the ratio of TOP/$Ni(acac)_2$ used in the synthesis. At low ratios (e.g., TOP/$Ni(acac)_2$ = 0.5 and 2.5), the formation of metallic Ni dominated, while at high ratios (e.g., TOP/$Ni(acac)_2$ = 11), uniform amorphous nickel phosphide nanoparticles were formed. A UV−vis study coupled with a DFT calculation verified the presence of Ni(0)-TOP_x complexes as intermediates in the synthesis. We further demonstrated the use of the highly uniform amorphous $Ni_{70}P_{30}$ nanoparticles as intermediates to obtain phase-pure $Ni_{12}P_5$, Ni_2P, and Ni_5P_4 with narrow size distribution through the modulation of reaction temperature alone. This method, by transforming uniform amorphous to crystalline nanoparticles, may expand to the nanoparticle syntheses of other metal compounds.

ASSOCIATED CONTENT

Supporting Information

The Supporting Information is available free of charge at https://pubs.acs.org/doi/10.1021/acs.inorgchem.4c03334.

ICP-MS results for the amorphous Ni_xP_y nanoparticles; particle size measured from TEM; LCF analysis of amorphous Ni_xP_y with different compositions; percentage composition of Ni and P derived from LCF; continuous Cauchy wavelet transform of a k^2-weight in R space and k-range of 3.3−12; plots of the real and imaginary components of the Ni K-edge EXAFS results; EXAFS modeling results for the amorphous Ni_xP_y and crystalline $Ni_{12}P_5$, Ni_2P, and Ni_5P_4 nanoparticles; TEM, XRD, and ICP-MS of nanoparticles synthesized with TOP/$Ni(acac)_2$ = 56 and 66; and UV−vis spectra of $Ni(COD)_2$ in TOP at different temperatures and the calculated spectrum of Ni(II)-TOP_4 (PDF)

AUTHOR INFORMATION

Corresponding Author

Jingyi Chen − *Department of Chemistry and Biochemistry, University of Arkansas, Fayetteville, Arkansas 72701, United States;* orcid.org/0000-0003-0012-9640; Email: chenj@uark.edu

https://doi.org/10.1021/acs.inorgchem.4c03334
Inorg. Chem. 2024, 63, 18981−18991

Authors

David Thompson − *Department of Chemistry and Biochemistry, University of Arkansas, Fayetteville, Arkansas 72701, United States*

Adam S. Hoffman − *Stanford Synchrotron Radiation Lightsource, SLAC National Accelerator Laboratory, Menlo Park, California 94025, United States*

Zachary R. Mansley − *Interdisciplinary Science Department, Brookhaven National Laboratory, Upton, New York 11973, United States;* orcid.org/0000-0002-1284-6316

Sarah York − *Department of Chemistry and Biochemistry, University of Arkansas, Fayetteville, Arkansas 72701, United States*

Feng Wang − *Department of Chemistry and Biochemistry, University of Arkansas, Fayetteville, Arkansas 72701, United States;* orcid.org/0000-0002-2740-3534

Yimei Zhu − *Condensed Matter Physics and Materials Science Department, Brookhaven National Laboratory, Upton, New York 11973, United States;* orcid.org/0000-0002-1638-7217

Simon R. Bare − *Stanford Synchrotron Radiation Lightsource, SLAC National Accelerator Laboratory, Menlo Park, California 94025, United States;* orcid.org/0000-0002-4932-0342

Complete contact information is available at: https://pubs.acs.org/10.1021/acs.inorgchem.4c03334

Notes

The authors declare no competing financial interest.

■ ACKNOWLEDGMENTS

J.C., D.T., and S.Y. acknowledge support from the U.S. National Science Foundation (NSF) under award number CHE-2304999. D.T. acknowledges support from the U.S. Department of Energy (DOE) Office of Science Graduate Student Research (SCGSR) Program. The XRD instrumentation was made possible by NIH P20 GM103429 from the IDeA Networks of Biomedical Research Excellence (INBRE) Program. HRTEM and EELS were carried out at Brookhaven National Laboratory (BNL) sponsored by the U.S. DOE Basic Energy Sciences (BES) and by the Materials Sciences and Engineering Division under Contract No. DE-SC0012704. Use of the Stanford Synchrotron Radiation Lightsource, SLAC National Accelerator Laboratory, is supported by the U.S. DOE BES under Contract No. DE-AC02-76SF00515. Co-ACCESS, part of the SUNCAT Center for Interface Science and Catalysis, is supported by the U.S. DOE, Office of Science, BES, Chemical Sciences, Geosciences, and Biosciences Division.

■ REFERENCES

(1) Oyama, S. T.; Gott, T.; Zhao, H.; Lee, Y.-K. Transition Metal Phosphide Hydroprocessing Catalysts: A Review. *Catal. Today* **2009**, *143*, 94−107.

(2) Prins, R.; Bussell, M. E. Metal Phosphides: Preparation, Characterization and Catalytic Reactivity. *Catal. Lett.* **2012**, *142*, 1413−1436.

(3) Golubeva, M. A.; Zakharyan, E. M.; Maximov, A. L. Transition Metal Phosphides (Ni, Co, Mo, W) for Hydrodeoxygenation of Biorefinery Products (a Review). *Pet. Chem.* **2020**, *60*, 1109−1128.

(4) Feng, L.; Xue, H. Advances in Transition-Metal Phosphide Applications in Electrochemical Energy Storage and Catalysis. *ChemElectroChem.* **2017**, *4*, 20−34.

(5) Bussell, M. E. New Methods for the Preparation of Nanoscale Nickel Phosphide Catalysts for Heteroatom Removal Reactions. *React. Chem. Eng.* **2017**, *2*, 628−635.

(6) Layan Savithra, G. H.; Muthuswamy, E.; Bowker, R. H.; Carrillo, B. A.; Bussell, M. E.; Brock, S. L. Rational Design of Nickel Phosphide Hydrodesulfurization Catalysts: Controlling Particle Size and Preventing Sintering. *Chem. Mater.* **2013**, *25*, 825−833.

(7) Callejas, J. F.; Read, C. G.; Roske, C. W.; Lewis, N. S.; Schaak, R. E. Synthesis, Characterization, and Properties of Metal Phosphide Catalysts for the Hydrogen-Evolution Reaction. *Chem. Mater.* **2016**, *28*, 6017−6044.

(8) Ray, A.; Sultana, S.; Paramanik, L.; Parida, K. M. Recent Advances in Phase, Size, and Morphology-Oriented Nanostructured Nickel Phosphide for Overall Water Splitting. *J. Mater. Chem. A* **2020**, *8*, 19196−19245.

(9) Banerjee, S.; Kakekhani, A.; Wexler, R. B.; Rappe, A. M. Relationship between the Surface Reconstruction of Nickel Phosphides and Their Activity toward the Hydrogen Evolution Reaction. *ACS Catal.* **2023**, *13*, 4611−4621.

(10) Park, J.; Koo, B.; Yoon, K. Y.; Hwang, Y.; Kang, M.; Park, J.-G.; Hyeon, T. Generalized Synthesis of Metal Phosphide Nanorods *via* Thermal Decomposition of Continuously Delivered Metal−Phosphine Complexes Using a Syringe Pump. *J. Am. Chem. Soc.* **2005**, *127*, 8433−8440.

(11) Henkes, A. E.; Vasquez, Y.; Schaak, R. E. Converting Metals into Phosphides: A General Strategy for the Synthesis of Metal Phosphide Nanocrystals. *J. Am. Chem. Soc.* **2007**, *129*, 1896−1897.

(12) Chiang, R.-K.; Chiang, R.-T. Formation of Hollow Ni_2P Nanoparticles Based on the Nanoscale Kirkendall Effect. *Inorg. Chem.* **2007**, *46*, 369−371.

(13) Henkes, A. E.; Schaak, R. E. Trioctylphosphine: A General Phosphorus Source for the Low-Temperature Conversion of Metals into Metal Phosphides. *Chem. Mater.* **2007**, *19*, 4234−4242.

(14) Wang, J.; Johnston-Peck, A. C.; Tracy, J. B. Nickel Phosphide Nanoparticles with Hollow, Solid, and Amorphous Structures. *Chem. Mater.* **2009**, *21*, 4462−4467.

(15) Zheng, X.; Yuan, S.; Tian, Z.; Yin, S.; He, J.; Liu, K.; Liu, L. One-Pot Synthesis of Hollow Nickel Phosphide Nanoparticles with Tunable Void Sizes Using Triphenylphosphine. *Mater. Lett.* **2009**, *63*, 2283−2285.

(16) Carenco, S.; Boissière, C.; Nicole, L.; Sanchez, C.; Le Floch, P.; Mézailles, N. Controlled Design of Size-Tunable Monodisperse Nickel Nanoparticles. *Chem. Mater.* **2010**, *22*, 1340−1349.

(17) Aso, K.; Hayashi, A.; Tatsumisago, M. Phase-Selective Synthesis of Nickel Phosphide in High-Boiling Solvent for All-Solid-State Lithium Secondary Batteries. *Inorg. Chem.* **2011**, *50*, 10820−10824.

(18) Muthuswamy, E.; Savithra, G. H. L.; Brock, S. L. Synthetic Levers Enabling Independent Control of Phase, Size, and Morphology in Nickel Phosphide Nanoparticles. *ACS Nano* **2011**, *5*, 2402−2411.

(19) Li, D.; Senevirathne, K.; Aquilina, L.; Brock, S. L. Effect of Synthetic Levers on Nickel Phosphide Nanoparticle Formation: Ni_5P_4 and NiP_2. *Inorg. Chem.* **2015**, *54*, 7968−7975.

(20) Pan, Y.; Liu, Y.; Zhao, J.; Yang, K.; Liang, J.; Liu, D.; Hu, W.; Liu, D.; Liu, Y.; Liu, C. Monodispersed Nickel Phosphide Nanocrystals with Different Phases: Synthesis, Characterization and Electrocatalytic Properties for Hydrogen Evolution. *J. Mater. Chem. A* **2015**, *3*, 1656−1665.

(21) García-Muelas, R.; Li, Q.; López, N. Initial Stages in the Formation of Nickel Phosphides. *J. Phys. Chem. B* **2018**, *122*, 672−678.

(22) Carenco, S.; Liu, Z.; Salmeron, M. The Birth of Nickel Phosphide Catalysts: Monitoring Phosphorus Insertion into Nickel. *ChemCatChem.* **2017**, *9*, 2318−2323.

(23) Popczun, E. J.; McKone, J. R.; Read, C. G.; Biacchi, A. J.; Wiltrout, A. M.; Lewis, N. S.; Schaak, R. E. Nanostructured Nickel Phosphide as an Electrocatalyst for the Hydrogen Evolution Reaction. *J. Am. Chem. Soc.* **2013**, *135*, 9267−9270.

(24) Manso, R. H.; et al. Revealing Structural Evolution of Nickel Phosphide-Iron Oxide Core−Shell Nanocatalysts in Alkaline Medium for the Oxygen Evolution Reaction. *Chem. Mater.* **2024**, *36*, 6440−6453.
(25) Murphy, I. A.; Rice, P. S.; Monahan, M.; Zasada, L. B.; Miller, E. M.; Raugei, S.; Cossairt, B. M. Covalent Functionalization of Nickel Phosphide Nanocrystals with Aryl-Diazonium Salts. *Chem. Mater.* **2021**, *33*, 9652−9665.
(26) Neese, F.; Wennmohs, F.; Becker, U.; Riplinger, C. The ORCA Quantum Chemistry Program Package. *J. Chem. Phys.* **2020**, *152*, 224108.
(27) Becke, A. D. A New Mixing of Hartree−Fock and Local Density-Functional Theories. *J. Chem. Phys.* **1993**, *98*, 1372−1377.
(28) Helmich-Paris, B.; de Souza, B.; Neese, F.; Izsák, R. An Improved Chain of Spheres for Exchange Algorithm. *J. Chem. Phys.* **2021**, *155*, 104109.
(29) Weigend, F.; Ahlrichs, R. Balanced Basis Sets of Split Valence, Triple Zeta Valence and Quadruple Zeta Valence Quality for H to Rn: Design and Assessment of Accuracy. *Phys. Chem. Chem. Phys.* **2005**, *7*, 3297−3305.
(30) Ravel, B.; Newville, M. Athena, Artemis, Hephaestus: Data Analysis for X-Ray Absorption Spectroscopy Using IFEFFIT. *J. Synchrotron Radiat.* **2005**, *12*, 537−541.
(31) Jette, E. R.; Foote, F. Precision Determination of Lattice Constants. *J. Chem. Phys.* **1935**, *3*, 605−616.
(32) Larsson, E. An X-Ray Investigation of the Ni-P System and the Crystal Structures of NiP and NiP_2. *Ark. Kemi* **1965**, *23*, 335−365.
(33) Carenco, S.; Labouille, S.; Bouchonnet, S.; Boissière, C.; Le Goff, X.-F.; Sanchez, C.; Mézailles, N. Revisiting the Molecular Roots of a Ubiquitously Successful Synthesis: Nickel(0) Nanoparticles by Reduction of [Ni(acetylacetonate)$_2$]. *Chem.—Eur. J.* **2012**, *18*, 14165−14173.
(34) Park, J.; et al. Monodisperse Nanoparticles of Ni and NiO: Synthesis, Characterization, Self-Assembled Superlattices, and Catalytic Applications in the Suzuki Coupling Reaction. *Adv. Mater.* **2005**, *17*, 429−434.
(35) Wang, D.; Li, Y. Effective Octadecylamine System for Nanocrystal Synthesis. *Inorg. Chem.* **2011**, *50*, 5196−5202.
(36) Moreau, L. M.; Ha, D.-H.; Bealing, C. R.; Zhang, H.; Hennig, R. G.; Robinson, R. D. Unintended Phosphorus Doping of Nickel Nanoparticles During Synthesis with TOP: A Discovery through Structural Analysis. *Nano Lett.* **2012**, *12*, 4530−4539.
(37) Moreau, L. M.; Ha, D.-H.; Zhang, H.; Hovden, R.; Muller, D. A.; Robinson, R. D. Defining Crystalline/Amorphous Phases of Nanoparticles through X-Ray Absorption Spectroscopy and X-Ray Diffraction: The Case of Nickel Phosphide. *Chem. Mater.* **2013**, *25*, 2394−2403.
(38) Yamamoto, T. Assignment of Pre-Edge Peaks in K-Edge X-Ray Absorption Spectra of 3d Transition Metal Compounds: Electric Dipole or Quadrupole? *X-Ray Spectrom.* **2008**, *37*, 572−584.
(39) Song, J.; Wei, Z.; Pan, Z.; Xie, Z.; Wei, S. Effect of Phosphorus Content on Local Structures of NiP Amorphous Alloys. *AIP Conf. Proc.* **2007**, *882*, 453−456.
(40) Duan, J.; Chen, S.; Ortíz-Ledón, C. A.; Jaroniec, M.; Qiao, S.-Z. Phosphorus Vacancies that Boost Electrocatalytic Hydrogen Evolution by Two Orders of Magnitude. *Angew. Chem., Int. Ed.* **2020**, *59*, 8181−8186.
(41) Chen, L.; Yu, C.; Song, X.; Dong, J.; Han, Y.; Huang, H.; Zhu, X.; Xie, Y.; Qiu, J. Microscopic-Level Insights into P-O-Induced Strong Electronic Coupling over Nickel Phosphide with Efficient Benzyl Alcohol Electrooxidation. *Small* **2024**, *20*, No. 2306410.
(42) Li, L.; Chen, F.; Zhao, B.; Yu, Y. Understanding of the Structural Evolution of Catalysts and Identification of Active Species during CO_2 Conversion. *Chin. Chem. Lett.* **2024**, *35*, No. 109240.
(43) Muñoz, M.; Argoul, P.; Farges, F. O. Continuous Cauchy Wavelet Transform Analyses of EXAFS Spectra: A Qualitative Approach. *Am. Mineral.* **2003**, *88*, 694−700.
(44) Boubnov, A.; Timoshenko, J.; Wrasman, C. J.; Hoffman, A. S.; Cargnello, M.; Frenkel, A. I.; Bare, S. R. Insight into Restructuring of Pd-Au Nanoparticles using EXAFS. *Radiat. Phys. Chem.* **2020**, *175*, 108304.
(45) Rundqvist, S.; Larsson, E. The Crystal Structure of $Ni_{12}P_5$. *Acta Chem. Scand. (1947−1999)* **1959**, No. 13, 551−560.
(46) Elfström, M. The Crystal Structure of Ni_5P_4. *Acta Chem. Scand. (1947−1999)* **1965**, No. 19, 1694−1704.
(47) Xu, Y. F.; Duchesne, P. N.; Wang, L.; Tavasoli, A.; Ali, F. M.; Xia, M.; Liao, J. F.; Kuang, D. B.; Ozin, G. A. High-Performance Light-Driven Heterogeneous CO_2 Catalysis with Near-Unity Selectivity on Metal Phosphides. *Nat. Commun.* **2020**, *11*, 5149.
(48) Seo, H.-R.; Cho, K.-S.; Lee, Y.-K. Formation Mechanisms of Ni_2P Nanocrystals using XANES and EXAFS Spectroscopy. *Mater. Sci. Eng., B* **2011**, *176*, 132−140.
(49) Pan, Y.; Chen, Y.; Lin, Y.; Cui, P.; Sun, K.; Liu, Y.; Liu, C. Cobalt Nickel Phosphide Nanoparticles Decorated Carbon Nanotubes as Advanced Hybrid Catalysts for Hydrogen Evolution. *J. Mater. Chem. A* **2016**, *4*, 14675−14686.
(50) Fujita, S.; Nakajima, K.; Yamasaki, J.; Mizugaki, T.; Jitsukawa, K.; Mitsudome, T. Unique Catalysis of Nickel Phosphide Nanoparticles to Promote the Selective Transformation of Biofuranic Aldehydes into Diketones in Water. *ACS Catal.* **2020**, *10*, 4261−4267.
(51) Fujita, S.; Yamaguchi, S.; Yamasaki, J.; Nakajima, K.; Yamazoe, S.; Mizugaki, T.; Mitsudome, T. Ni_2P Nanoalloy as an Air-Stable and Versatile Hydrogenation Catalyst in Water: P-Alloying Strategy for Designing Smart Catalysts. *Chem.—Eur. J.* **2021**, *27*, 4439−4446.
(52) Yamaguchi, S.; Fujita, S.; Nakajima, K.; Yamazoe, S.; Yamasaki, J.; Mizugaki, T.; Mitsudome, T. Air-Stable and Reusable Nickel Phosphide Nanoparticle Catalyst for the Highly Selective Hydrogenation of D-Glucose to D-Sorbitol. *Green Chem.* **2021**, *23*, 2010−2016.
(53) Kong, S.; et al. Probing of the Noninnocent Role of P in Transition-Metal Phosphide Hydrogen Evolution Reaction Electrocatalysts via Replacement with Electropositive Si. *Chem. Mater.* **2023**, *35*, 5300−5310.

https://doi.org/10.1021/acs.inorgchem.4c03334
Inorg. Chem. 2024, 63, 18981−18991